

ICESat measurements of sea ice freeboard and estimates of sea ice thickness in the Weddell Sea

H. Jay Zwally,¹ Donghui Yi,² Ron Kwok,³ and Yunhe Zhao⁴

Received 29 March 2007; revised 12 October 2007; accepted 9 November 2007; published 19 February 2008.

[1] Sea ice freeboard heights in the Weddell Sea of Antarctica are derived from the Ice, Cloud, and Land Elevation Satellite (ICESat) laser altimeter measurements, which have a unique range precision to flat surfaces of 2 cm within 70 m footprints spaced at 172 m along track. Although elevations of flat surfaces can be obtained to an accuracy of ~ 10 cm (1σ) per footprint, direct determination of freeboard heights is precluded by errors in knowledge of the geoid and temporal variability of the ocean surface. Therefore freeboards are determined relative to an ocean reference level detected over areas of open water and very thin ice within the sea ice pack using an along-track filtering method. The open water/thin ice selections show good agreement in the combined analysis of ICESat segments and Envisat Synthetic Aperture Radar (SAR) imagery. The average residual between the ICESat-measured ocean level and the EGM96 geoid is 1.4 m. Estimates of snow depth on the sea ice from AMSR-E passive microwave data along with nominal densities of snow, water, and sea ice are used to estimate sea ice thickness. Four periods of ICESat data in May–June (fall) and October–November (late winter) of 2004 and 2005 between longitudes 298°E and 360°E are analyzed. In the fall the mean freeboards are 0.28 m in 2004 and 0.29 m in 2005, and the mean thicknesses are 1.33 m in 2004 and 1.52 m in 2005. In late winter the freeboards grew to 0.37 m in 2004 and 0.35 in 2005, and the thicknesses grew to 2.23 m in 2004 and 2.31 m in 2005. The interannual differences in freeboard are small, and the larger interannual change in estimated thickness mainly represents differences in the snow depth estimates. Seasonal changes in the spatial patterns of freeboard and thickness over the 4 months correlate with the expected circulation of sea ice in the Weddell Sea, as indicated by sea ice velocity fields.

Citation: Zwally, H. J., D. Yi, R. Kwok, and Y. Zhao (2008), ICESat measurements of sea ice freeboard and estimates of sea ice thickness in the Weddell Sea, *J. Geophys. Res.*, 113, C02S15, doi:10.1029/2007JC004284.

1. Introduction

[2] Sea ice and snow cover affect the exchange of heat, energy, mass, and momentum between the atmosphere and the ocean [Strass and Fahrbach, 1998]. Both the mixed layer of the ocean and the boundary layer of the atmosphere are strongly influenced by the behavior of the sea ice and snow covers [Martinson, 1990; Hartmann et al., 1994]. Since satellite-borne passive microwave observations became available in the early 1970s, significant progress has been made in the study of snow and sea ice of the polar regions. Currently, sea ice concentration, extent, motion, deformation, surface temperature, and snow depth can all be monitored

routinely from satellites [Gloersen et al., 1992; Markus and Cavalieri, 1998; Comiso et al., 2003; Bamber and Kwok, 2004]. These remote sensing data sets have contributed to the understanding of Southern Ocean sea ice processes, air-sea interactions, and the spatial and temporal variability of the ice pack [Drinkwater and Lytle, 1997; Zwally et al., 2002b; Kwok and Comiso, 2002; Kwok, 2005; Geiger and Drinkwater, 2005]. Information on sea ice thickness is crucial for the quantitative understanding of the physical processes of the polar oceans. To date, measurements of sea ice freeboard and thickness in the Southern Ocean have been very limited. Knowledge of Antarctic sea ice freeboard and thickness has been mainly based on information from surface and ship-based measurements [Ackley, 1979; Wadhams et al., 1987; Lange and Eicken, 1991; Strass and Fahrbach, 1998; Drinkwater et al., 2001; Tin and Jeffries, 2001; Worby et al., 2001]. Also, the sampled areas were mostly at the margins of the Antarctic sea ice pack that is accessible by ships. Therefore available sea ice thickness results tend to be from the thin end of the thickness distribution.

[3] In January 2003, NASA launched Ice, Cloud, and Land Elevation Satellite (ICESat) with a precision laser altimeter system for measuring surface elevations [Zwally et

¹Cryospheric Sciences Branch, Goddard Space Flight Center, Greenbelt, Maryland, USA.

²SGT, Incorporated, Cryospheric Sciences Branch, Goddard Space Flight Center, Greenbelt, Maryland, USA.

³Jet Propulsion Laboratory, California Institute of Technology, Pasadena, California, USA.

⁴Caelum Research Corporation, Oceans Sciences Branch, Goddard Space Flight Center, Greenbelt, Maryland, USA.

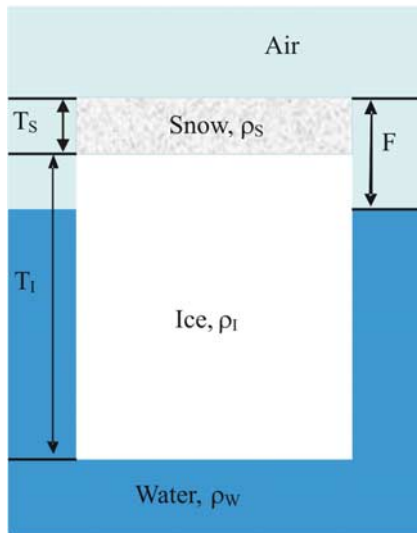


Figure 1. Snow-covered sea ice. Freeboard (F) is defined as the total height of the snow cover and sea ice above the ocean. If the snow cover thickness (T_s) becomes equal to F in areas of large snow cover, then sea ice thickness (T_i) includes (1) the sea ice formed from frozen ocean water and (2) the subocean snow cover and sea ice mixture formed from ocean water flooding the submerged snow. Nominal densities used to estimate sea ice thickness as a function of F are $\rho_s = 300 \text{ kg m}^{-3}$, $\rho_w = 1023.9 \text{ kg m}^{-3}$, and $\rho_i = 915.1 \text{ kg m}^{-3}$.

al., 2002a]. The precision of ICESat measurements of mean surface elevations of flat surfaces is 2 cm over 70 m laser footprints spaced at 172 m [Kwok *et al.*, 2004], providing a powerful new tool for studying sea ice freeboard and thickness. The ICESat orbit extends to polar latitudes of 86° , and provides coverage of all sea ice in the Southern Ocean surrounding Antarctica and most of the sea ice in the Arctic Ocean.

[4] In this paper, we derive sea ice freeboards from ICESat elevation profiles and estimate sea ice thicknesses over the Weddell Sea for four ICESat survey periods: 18 May to 20 June 2004 (MJ 2004), 4 October to 8 November 2004 (ON 2004), 20 May to 23 June 2005 (MJ 2005), and 21 October to 24 November 2005 (ON 2005). Our method of deriving freeboards uses segments of open water and thin ice detected by the laser altimeter to determine the height of the along-track ocean surface, which is then used as the ocean reference level for the freeboard heights (F in Figure 1) of the snow-covered sea ice. Our F is defined as the total height of the snow cover and sea ice above the ocean, whereas the term freeboard is sometimes used to refer to only the sea ice portion leading to the possibility of so-called negative freeboards. After determining the ocean reference level for each ICESat along-track elevation measurement, the freeboard height is determined relative to this reference level. The ICESat detection of open water and thin ice areas is validated by comparison with available Envisat Synthetic Aperture Radar (SAR) images that show leads and polynyas with thin ice and open water.

[5] Estimation of sea ice thickness (T_i) from the freeboards requires additional information and/or a number of

assumptions about the densities and relative thicknesses of the snow cover and the sea ice, similar to estimations of sea ice thickness from radar altimetry [Laxon *et al.*, 2003] and submarine sonar measurement of sea ice drafts [Rothrock *et al.*, 1999]. While our freeboard values are derived from a direct ICESat measurement, the estimation of the corresponding sea ice thickness is much less definitive. Even the definition of sea ice thickness is ambiguous if the weight of the snow cover is sufficient to depress the actual sea ice below the ocean level, which may be a frequent occurrence in the Antarctic ice pack. In that case, we define sea ice thickness (T_i) to include both (1) the sea ice formed from frozen ocean water and (2) the snow and sea ice mixture formed from ocean water flooding of the submerged snow.

[6] The purpose of this paper is not to provide a definitive solution of the problem of deriving sea ice thickness from either freeboards or drafts. Our objective is to provide an estimate of sea ice thickness as a function of the measured F based on nominal values of snow, water, and sea ice densities, and snow depth data from AMSR-E [Markus and Cavalieri, 1998]. The sea ice thickness estimates obtained are compared with measurements from field programs in the Weddell Sea. The spatial distribution patterns of freeboard and thickness are compared with sea ice velocity fields generated from AMSR-E brightness temperatures, showing seasonal changes in the distributions consistent with the drift of the ice pack as well as growth. Improved information on snow cover and values of the densities would clearly provide better estimates of sea ice thickness, but our present knowledge of these parameters is poor at best.

[7] The paper is organized as follows. Data on ICESat elevations and AMSR-E snow depths and ice concentrations are described in section 2. In section 3, we present our techniques to determine ocean levels and sea ice freeboards from ICESat profiles and compare near-coincident ICESat elevation profiles with Envisat images in the Weddell Sea. Freeboard maps are derived and converted to thickness and compared with available measurements in Section 4. The comparison of ICESat measured ocean levels and EGM96 geoid is discussed in section 5. Ice motion and its relationship with freeboard and thickness are discussed in section 6. As this represents an initial examination of using ICESat elevations and AMSR-E snow depths to estimate sea ice thickness, the limitations and outstanding issues are discussed in section 7. Section 8 summarizes the paper.

2. Data Description

[8] ICESat determines the range from spacecraft to the surface by measuring the time delay between the transmission of the laser pulse and the detection of the echo waveform from the surface. The portion of the echo waveform corresponding to the reflections from the surface is digitized in 1 ns (15 cm) range bins. The echo waveforms have 544 range bins over ice sheets and land and 200 range bins over ocean and sea ice. The wider waveform window was chosen for ice sheets and land because of their more complex surface features, such as large surface slopes and thick canopies. The quality of the waveform is important in determining surface elevation. The ICESat laser transmitted

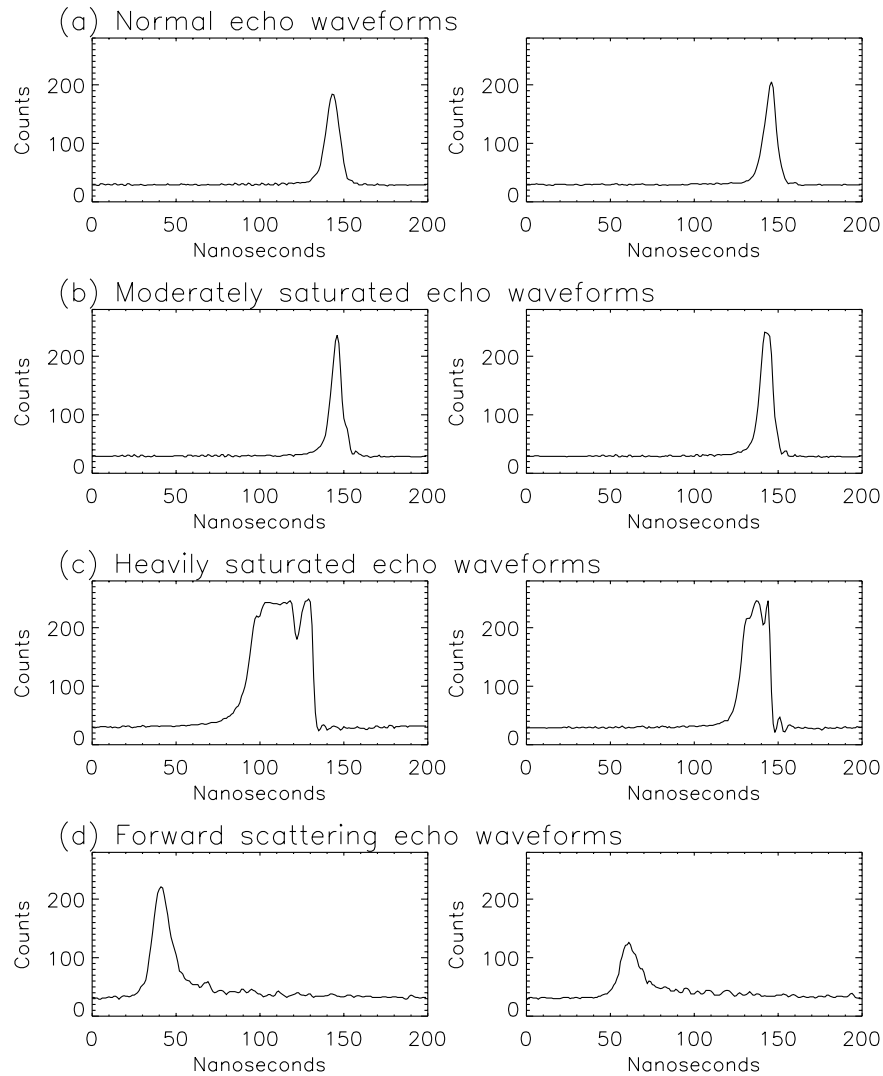


Figure 2. Ice, Cloud, and Land Elevation Satellite (ICESat) 1064 nm sample waveforms over sea ice. (a) Normal unsaturated waveforms. (b) Normal slightly saturated waveforms; the range delay can be corrected for this type of waveforms. (c) Heavily saturated waveforms. Flat tops and wide pulses indicate the waveforms are heavily saturated. More works are needed to apply saturation correction to this type of waveforms. (d) Forward scattering waveforms. Long trailing edge of the waveforms indicates forward scattering.

waveforms are very stable and introduce little error in elevation calculations. From preflight ground tests, Yi *et al.* [2003] estimated a range uncertainty of 2.0 cm due to the combined effects of the variation of transmitted waveforms, flat surface echo waveforms, and using a Gaussian fitting procedure of ICESat waveform analysis. In orbit, the echo waveforms are additionally affected by the transmitted pulse energy, atmospheric (including cloud) attenuation, surface reflectivity, slope, and roughness within the laser footprint, all of which affect the accurate location of surface elevation. However, the 2.0 cm range precision estimated preflight has been confirmed by analysis of a 2 cm noise level in ranges over segments of flat ice sheet surfaces and sea ice polynya [Kwok *et al.*, 2004; Shuman *et al.*, 2006] The transmitted power of ICESat's lasers decreases with age. At the beginning of life of each of the three ICESat lasers, the received waveforms were typically saturated over snow surfaces.

Thin ice or rough open water has lower reflectivity than snow, so the waveforms over those surfaces are only moderately saturated. However, flat surfaces can produce strong specular reflections and make the echo waveforms heavily saturated. For each laser shot, the detector gain of the GLAS instrument is automatically adjusted on the basis of the pulse amplitudes of the previous laser shots. The gain is lowered when the expected echo waveform amplitude becomes higher. Sudden increases in surface reflectivity can also cause the echo waveforms to be saturated when there is a lag in detector gain response. Typically, that happens at abrupt transitions from a rougher water surface to a snow surface.

[9] Four examples of echo waveforms are shown in Figure 2. Figure 2a shows normal echo waveforms. Saturated waveforms (Figures 2b and 2c) delay the apparent return energy, increase the range estimates, and make the

surface appear lower when applying the standard waveform fitting procedure. To compensate for this delay, a saturation correction is applied to moderately saturated waveforms (Figure 2b) to improve the accuracy of surface elevation [Sun *et al.*, 2003; Yi *et al.*, 2005]. The saturation corrections used in this study have been applied to all ICESat products starting with Release 28. In this study, heavily saturated waveforms (Figure 2c) are filtered out on the basis of their pulse width and reflectivity.

[10] In addition, clouds attenuate the laser signal and also scatter laser photons, making the photons travel a longer path thus introducing a bias in the derived elevations. The delayed return energy appears in the trailing edge of the echo waveforms. Depending on cloud type, this forward scattering (Figure 2d) could introduce errors larger than 1 m [Mahesh *et al.*, 2002]. In this study, a limit of 80 counts (100 counts for MJ 2004) is applied to the detector gain to filter out the stronger atmospherically attenuated waveforms. We define a pulse-broadening parameter S ,

$$S = \frac{c}{2} \sqrt{\sigma_R^2 - \sigma_T^2},$$

where σ_R is the echo waveform 1-sigma pulse width, σ_T is the transmitted waveform 1-sigma pulse width, and c is the speed of light. S measures the broadening of the transmitted pulse associated with surface topography and the undesirable effects of saturation and atmospheric forward scattering. Heavily saturated waveforms and forward scattering waveforms have broadened pulse widths, so data with S larger than 0.8 m are discarded. Heavily saturated waveforms also tend to have very high apparent reflectivity, and forward scattering waveforms tend to have low reflectivity. Therefore data with reflectivity less than 0.05 and larger than 0.9 are also discarded.

2.1. ICESat Surface Elevation

[11] The ICESat measured surface elevation H_{ie} , (i_elev in product GLA06, see <http://nsidc.org/data/gla06.html>) is referenced to an Earth ellipsoid with equatorial radius = 6378136.3 m and flattening = 1/298.257 [Schutz *et al.*, 2005]. ICESat surface elevations have instrument corrections, dry and wet troposphere corrections, and tidal corrections applied. The global ocean model used is GOT99.2 [Ray, 1999]. The Geoid model used is EGM96.

[12] Sea surface response to atmospheric pressure loading, the inverse barometer effect, is computed using the method described in the AVISO and PODACC user handbook (http://podaac-www.jpl.nasa.gov/jason/documents/Handbook_Jason_v2-1.pdf) [Picot *et al.*, 2003]. The inverse barometer correction ΔH_{ib} is a function of surface atmospheric pressure P_{atm} and P , the time varying mean of the global surface atmospheric pressure over the oceans,

$$\Delta H_{ib} = 9.948 \times (P_{atm} - P).$$

ΔH_{ib} is applied to the ICESat elevation at the same time as the saturation correction.

[13] The surface atmospheric pressures used here are from National Center for Environmental Prediction (NCEP) [Stackpole, 1993]. The mean global surface atmospheric pressures over the ocean are from <ftp://ftp.cls.fr/pub/oceano/>

calval/pression/moy_globale_spatiale.txt [Dorandeu and Le Traon, 1999]. The relationship between ICESat elevations and time-varying sea level pressure was examined by Kwok *et al.* [2006]. They showed that the Arctic Ocean, to first order, behaves close to the relationship described by the above equation.

[14] In the following analysis, we define the elevation, h , above the geoid as

$$h = H_{ie} + \Delta H_{ib} + \Delta H_{sat} - h_g,$$

where ΔH_{sat} is the saturation correction and h_g is the EGM96 geoid height. Note that the influence of ΔH_{ib} , ΔH_{sat} , and h_g are removed from H_{ie} , but other factors such as dynamic topography and the residuals in the static geoid still affect h .

2.2. AMSR-E Snow Depth and Ice Concentration

[15] Estimation of sea ice thickness from freeboard requires knowledge of snow loading. The snow cover over the Antarctic sea ice is extremely heterogeneous, being composed of new snow, soft slabs, depth hoar, icy layers and slush. Often, all are present at a single location [Sturm *et al.*, 1998]. Recently, Markus and Cavalieri [1998] developed an algorithm for estimating the snow depth on sea ice over the Southern Ocean from passive microwave measurements. Their algorithm is based on combining DMSP SSM/I 19 GHz and 37 GHz brightness temperatures to estimate snow depth on sea ice from these simultaneous observations. The algorithm is applicable only to a dry snow cover and has an upper limit of 0.5 m for snow depth retrievals. When the snow is wet, the emissivity of snow increases more at 37 GHz than at 19 GHz, leading to an incorrect (underestimate of) snow depth. An identical algorithm has been applied to AMSR-E data to derive snow depth over Antarctic sea ice [Comiso *et al.*, 2003]. We use these AMSR-E derived snow depths to compute snow loading. Clearly, the limitations and uncertainties of these snow depth estimates affect the accuracy of the estimated sea ice thickness. For a given freeboard, an underestimated snow depth will give an overestimate of sea ice thickness and vice versa; similarly, for areas with snow depth over 0.5 m, the sea ice thickness would be overestimated.

[16] Figure 3 shows the AMSR-E mean snow depth maps and histograms for the four periods. While the snow depths are less than 0.5 m in most areas and at most times, in a few areas snow depths are larger than 0.5 m in the May–June periods of 2004 and 2005. In the May–June periods, the snow layers are thicker in the west Weddell Sea than in the east. In the October–November periods, they are thicker in the northwest than in the southeast.

[17] In this study, AMSR-E daily sea ice concentrations [Comiso *et al.*, 2003] are used to separate open ocean and sea ice. Because of atmospheric attenuation, the ICESat measured surface reflectivity is not the true reflectivity of the surface. Although reflectivities of open water and thin ice are generally lower than that of snow surfaces [Kwok *et al.*, 2006], in general the surface reflectivity cannot be used to differentiate between snow, ice, and open water surfaces unambiguously, because the atmospheric condition can modify the apparent surface reflectivity. To avoid open ocean and the low accuracy of snow depth in low ice

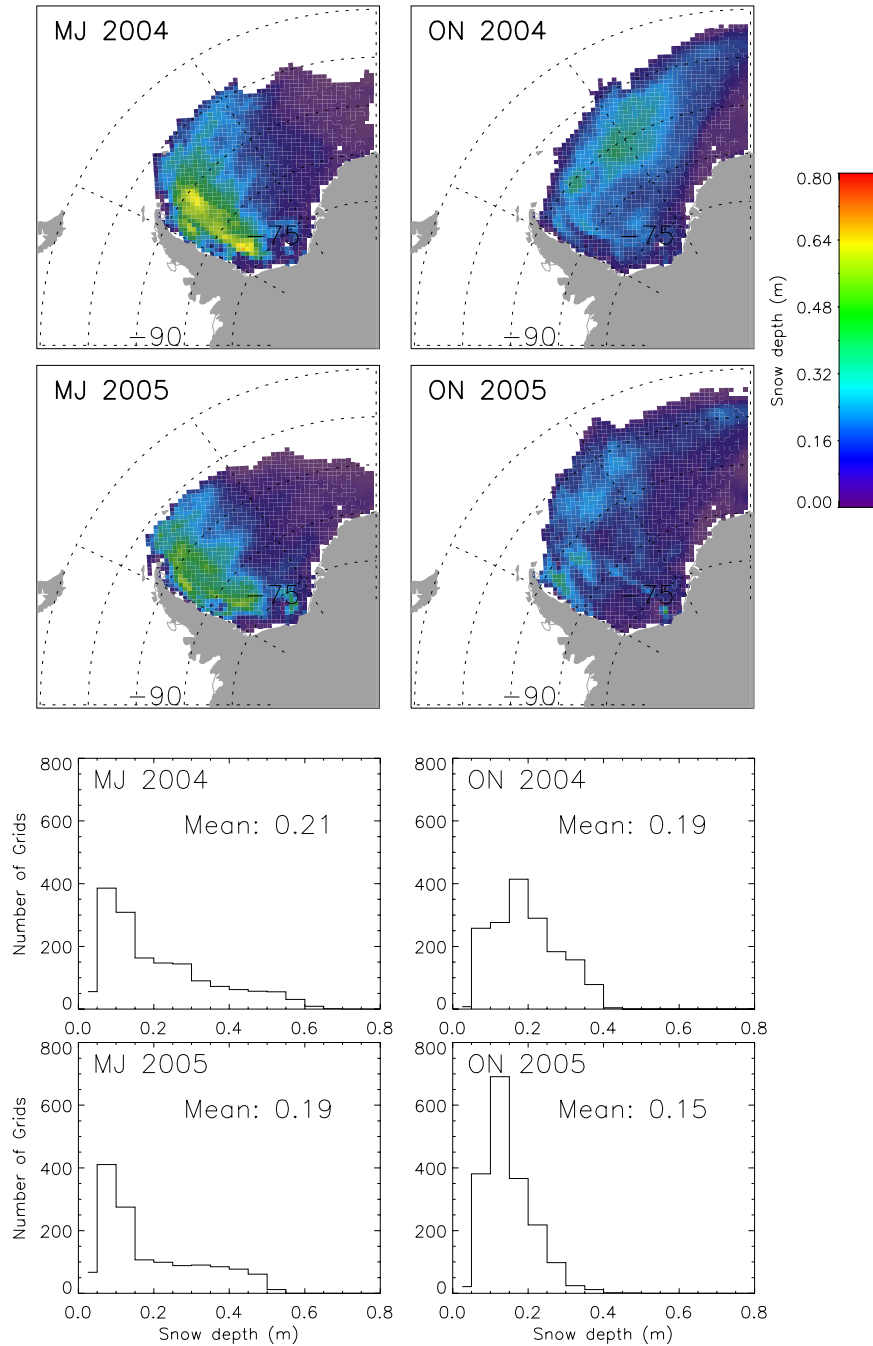


Figure 3. Mean snow depth maps and histograms from AMSR-E for the four periods. Mean snow depths for the four periods are 0.21, 0.19, 0.19, and 0.15 m.

concentration areas, a strict ice concentration limit is used: data with ice concentration less than 60% are discarded. All data shown in this paper are in areas with sea ice concentration greater than 60%. Figure 4 shows AMSR-E mean sea ice concentration maps and histograms for the four periods. The mean concentrations are $\sim 93\%$ for all four periods.

3. Derived Ocean Levels and Freeboard Heights

[18] ICESat measures a surface elevation profile referenced to an ellipsoid. Because of the limited accuracy

of the geoid and ocean tide models, and poor knowledge of the dynamic topography over the Southern Ocean, sea ice surface elevation referenced to a geoid cannot be regarded as sea ice freeboard. Figure 5 shows profiles of surface height referenced to geoid (h) along a ground track (track 39) for three different ICESat campaign periods. The elevation varies from -2 to 4 m. The large variation in these profiles clearly indicates that h is not a direct measurement of sea ice freeboard. Similar patterns of variation of the three profiles suggest that the main component of the variation is due to residuals in the static geoid. The smaller, time-varying portion of h , other than the sea ice

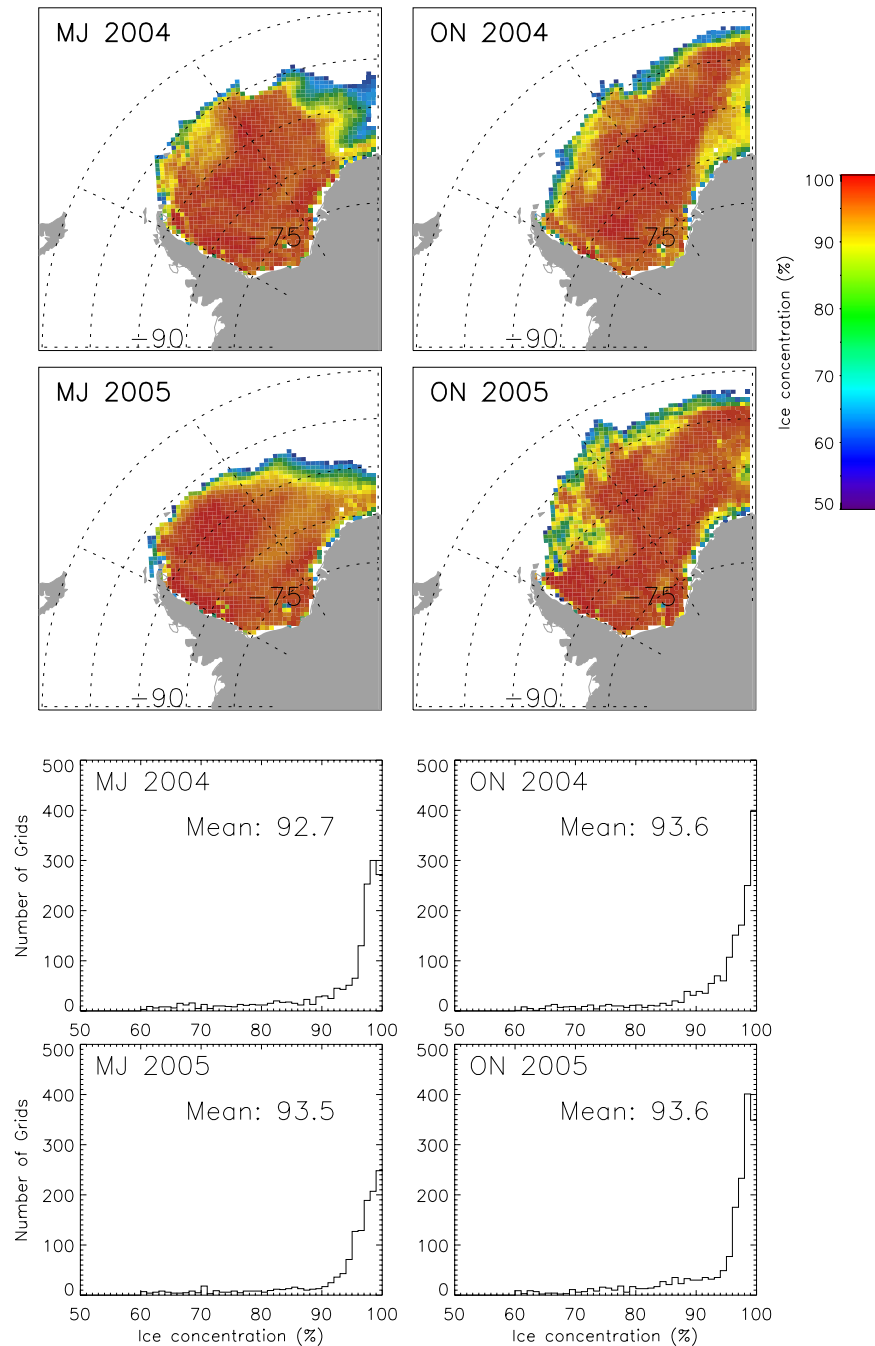


Figure 4. AMSR-E mean ice concentration maps and histograms for the four periods. Mean ice concentrations for the four periods are 92.7%, 93.6%, 93.5%, and 93.6%.

freeboard variation, is likely due to tidal error, dynamic ocean topography, and ICESat laser pointing error.

[19] The information needed to calculate sea ice freeboard is the elevation difference between the top of the snow surface on the sea ice and local ocean levels (Figure 1). If the elevation difference is known, even if the absolute elevations are biased, the sea ice freeboard can be determined. Thus the knowledge of relative elevation is crucial while absolute elevation is less important. This is the underlying concept in the derivation of freeboard. Here we describe an algorithm to determine relative elevation and use this relative elevation to estimate sea ice freeboard.

By determining local ocean level and using only the relative elevation, the influence of the longer-wavelength (>50 km) factors, such as geoid error, long-wavelength laser pointing error, and tidal error, which affect the absolute elevation, are removed from the freeboard calculation.

3.1. Ocean Level From ICESat Profiles

[20] To demonstrate the ocean level selection and freeboard calculation algorithm, we use a 330 km elevation profile over the Weddell Sea from the October–November 2003 period (Figure 6). Figure 6a shows that the elevation referenced to the geoid varies by more than 3 m. To remove

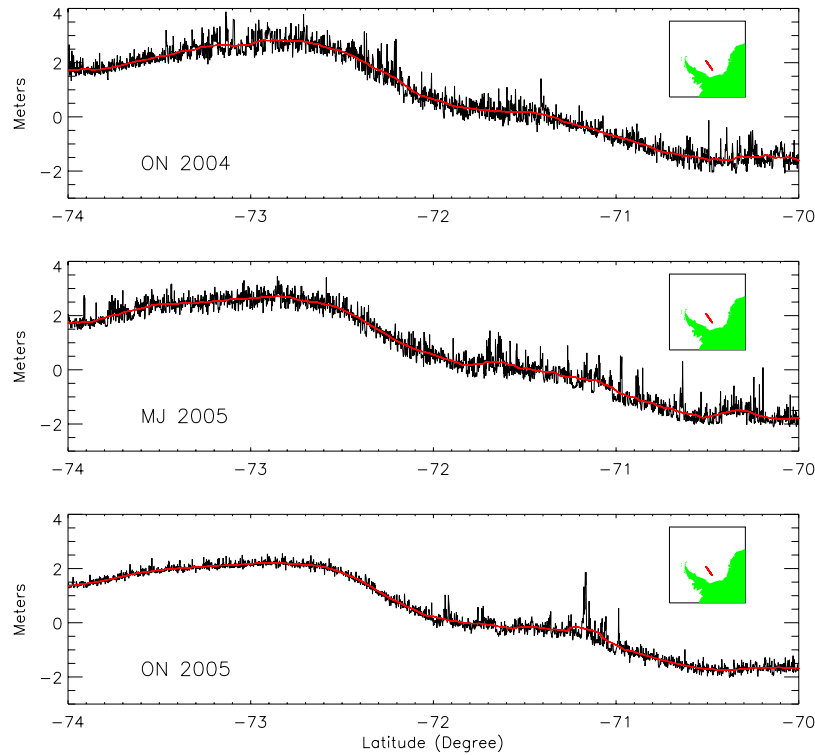


Figure 5. ICESat elevation profiles of Track 39 over the Weddell Sea for three different operation periods. The 25 km running means are the red lines in the profiles. Locations of the profiles are shown in the maps.

the long-wavelength geoid error, tidal error, and dynamic ocean topography, we calculate a 20 km running mean (h_m), which is then used as a reference level to compute relative elevations. This relative elevation, h_r , with respect to the 20 km running means is given by

$$h_r = h - h_m.$$

Next, we need to determine the reference ocean level from this h_r profile (Figure 6b).

[21] In this study, leads (open water and thin ice) in the sea ice are considered to be at ocean level. A lead is a long, narrow, opening in pack ice, which may be covered by thin ice. *Lindsay and Rothrock* [1995] found that leads cover 2% to 3% of the surface area in the central Arctic in the winter and 5% to 7% in the summer. In the Arctic peripheral seas, leads cover 6% to 9% of the surface areas in winter. Winter ice concentration is lower in the Southern Ocean than in the Arctic Ocean [*Gloersen et al.*, 1992]. For areas where the sea ice concentration is larger than 60%, the average sea ice concentration is around 93% (see Figure 4).

[22] Here, we assume that ICESat can detect open water or thin ice in at least 2% (6 of its 300 samples) in a 50 km section of a profile. Ocean level, h_s , at any given point is determined by averaging the lowest 2% of the h_r values within ± 25 km of that point (Figure 7). The 2% value was selected empirically. It provides enough points in calculating mean ocean level to reduce measurement noise, and also minimizes the influence of thinner ice on the calculation. This value may be optimized further as we learn more about the distribution of leads in the Southern Ocean. In extreme

cases when there is no open water within the 50-km range, h_s will measure the height of thin ice, thus underestimating freeboard (see section 7 for more discussion). Since islands or icebergs may appear in the profile, data with h larger than 4 m are discarded to avoid their influence.

3.2. Freeboard

[23] Freeboard height, F , at a given point is defined as,

$$F = h_r - h_s.$$

To have a valid F at a point, there must be enough valid elevation measurements available within ± 25 km of that point. In this study, a point is discarded if less than 50% (150 points) of the total 300 points are available.

[24] Freeboards calculated for the profile in Figure 6a are shown in Figure 6c. The histogram of the freeboards in Figure 6g shows a typical asymmetrical freeboard distribution with a sharp increase in the leading edge and a slow decrease in the tail of the distribution. The mean freeboard of this section is 0.43 m. The peak of the histogram (mode) occurs around 0.23 m, approximately half of the mean value. Since the mean of the lowest 2% of the elevations is used to determine ocean level, $\sim 1\%$ of the F values will be negative.

[25] The pulse-broadening parameter S is shown in Figure 6d. Low S values (~ 0.3) indicate no saturation, no cloud forward scattering, and a relatively smooth surface. Figure 6h shows the histogram of S . The mean S of this section is 0.41 m. Figure 6e shows the gain values. Most of the gains are at 13 counts, and all of the gains are below 20 counts in this profile. Large gain values (≥ 80) are often

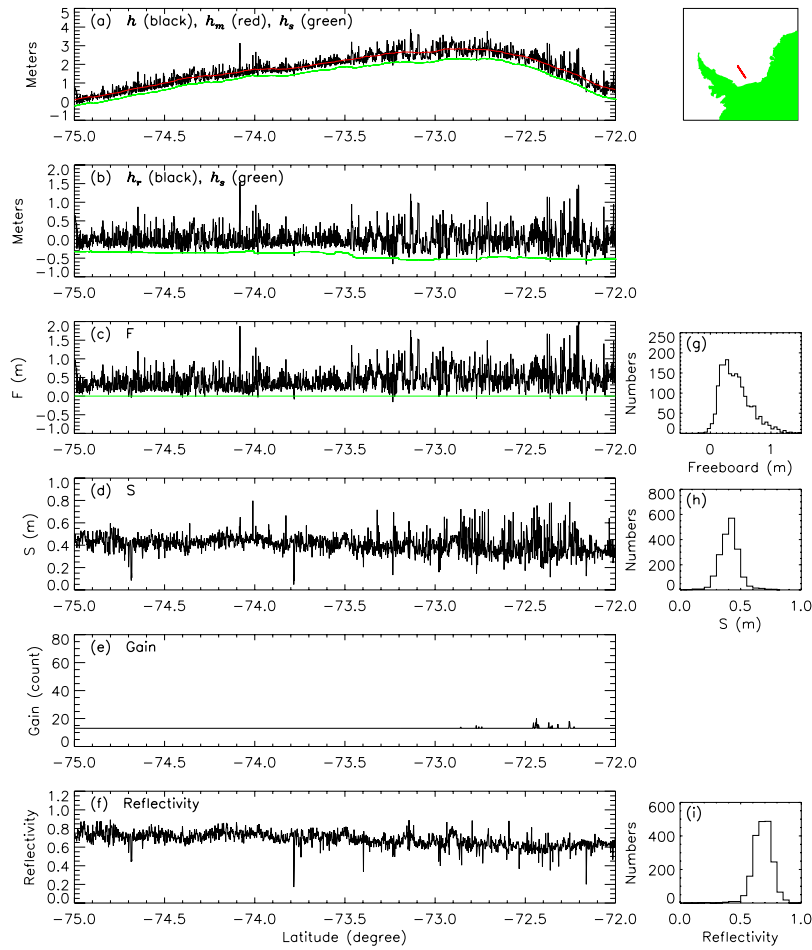


Figure 6. A sample of ICESat elevation profile over the Weddell Sea from ON 2003 period: (a) h and its 20 km running mean h_m ; (b) h_r and h_s ; (c) freeboard; (d) pulse-broadening parameter S ; (e) detector gain; (f) reflectivity; (g) histogram of freeboard: Mean is 0.43 m; (h) histogram of S : Mean is 0.41 m; (i) histogram of reflectivity: Mean is 0.68.

associated with clouds. The ICESat 1064-nm cloud channel measures cloud heights [Abshire *et al.*, 2005]; it shows no clouds in this profile, consistent with all gain values being low. Figures 6f and 6i show the profile and histogram of reflectivity. The mean reflectivity is 0.68. Variations in S , gain, and reflectivity are important because these parameters are related to the quality of the return waveforms and can be used to filter out data from heavily saturated and forward scattering waveforms. In general, data with low S , low gain, and moderate reflectivity are of high quality.

[26] There is a maximum of 300 elevation measurements over each 50 km section of a profile. Histograms of h_r at 20 points from Figure 6b, separated by 2 seconds (13.3 km), are shown in Figure 7. Each histogram shows the distribution of h_r for the segment extending 25 km to either side of the point, and includes 300 points. The green lines mark the selected ocean level, i.e., the mean of the lowest 2% of h_r . The selected ocean level is used to calculate freeboard F at that point. There are two distinct types of histograms in Figure 7. The broader, more symmetric distributions (the top two rows, more equatorward) may represent mixed ice types with young, first year and multiyear sea ice. The narrower, asymmetric distribution (the bottom two rows,

more poleward) may represent sea ice mainly from young and first year ice since they are mostly less than 0.5 m. The distributions in the third row are in transition. Where ice concentrations are lower, the histograms sometimes show two separate peaks; one from open water/thin ice and the other from thicker ice.

3.3. Comparison With Envisat SAR

[27] Open water and thin ice have the lowest elevation in an elevation profile. Kwok *et al.* [2004, 2006] showed several examples of near-coincident ICESat elevation and RADARSAT images over the Arctic. Likewise, we located a number of near-coincident Envisat SAR images and ICESat profiles over the Weddell Sea. Figure 8 is an example of several new opening/thin ice segments identified in an Envisat image near-coincident with an ICESat profile. Note the coincidence between the openings in the Envisat image (dark areas) and the places where $h_r = h_s$ in Figure 8a. The thin ice on the left side between 6 and 11 km is shown on the image. Since there is a time difference of 12 h between the Envisat image and the ICESat profile, the features on the image do not match the profile exactly. Nevertheless, it shows our method correctly selected the open water/thin ice samples as ocean level reference.

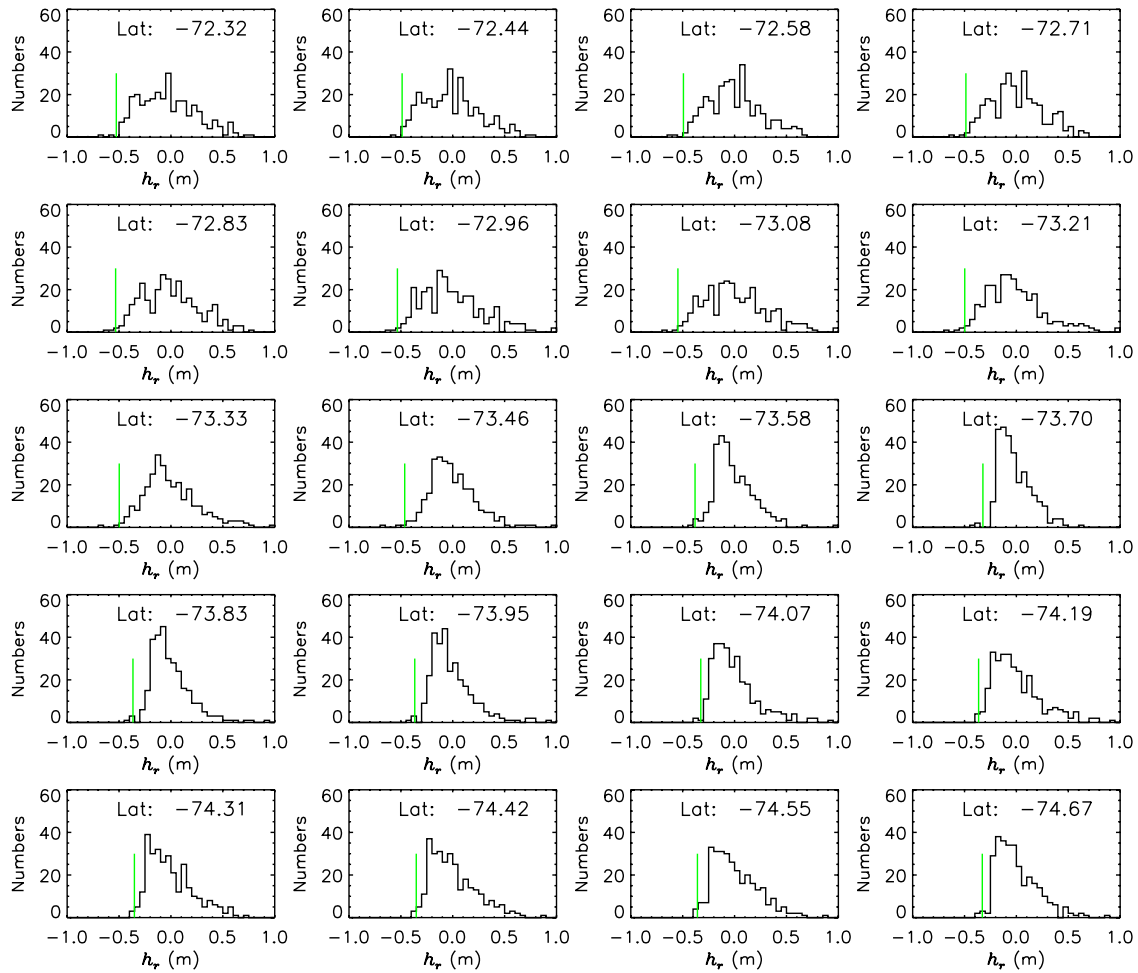


Figure 7. The h_r histograms at twenty points evenly distributed along the profile in Figure 6b. Green line in each histogram is the selected ocean level (h_s). Latitude is where the sample point located along the profile.

Figures 8b–8e show that low freeboard is generally associated with low pulse broadening (small S), higher detector gain, and low reflectivity. Since there are few coincident satellite SAR images and ICESat profiles available during these periods, this approach of using overlapping imagery and elevation profiles cannot be used routinely to determine ocean level along an ICESat ground track.

4. Sea Ice Thickness

[28] Sea ice thickness T_I is a function of freeboard height F , snow depth T_S , snow density ρ_S , water density ρ_W , and sea ice density ρ_I (see Figure 1), according to Archimedes buoyancy principle,

$$T_I = \frac{\rho_W}{\rho_W - \rho_I} F - \frac{\rho_W - \rho_S}{\rho_W - \rho_I} T_S.$$

[29] In this study, constant densities of $\rho_S = 300 \text{ kg m}^{-3}$, $\rho_W = 1023.9 \text{ kg m}^{-3}$, and $\rho_I = 915.1 \text{ kg m}^{-3}$ are used to calculate sea ice thickness from the freeboard. T_I can then be expressed as

$$T_I = 9.411 \times F - 6.653 \times T_S.$$

Massom et al. [1997] reported a mean snow density of $320 \pm 90 \text{ kg m}^{-3}$ from a winter cruise study in the Weddell Sea. We chose 300 kg m^{-3} since the maximum frequency is between 250 kg m^{-3} and 350 kg m^{-3} . Implicit in the above equation is that there is a distinct interface between the snow and sea ice. Compared to the Arctic, the interface is expected to be more complex because of flooding and snow-ice formation. We also recognize that ice thickness is sensitive to the local and regional variability of snow and ice densities. Since we have no detailed information about the errors in local densities, the error in T_I is not estimated. Again, the purpose of this paper is not to provide a definitive solution of the problem of deriving sea ice thickness from either freeboards or drafts but only an assessment of the results using nominal values of the above parameters. We will return to these issues in our discussion.

[30] Sea ice freeboard is calculated for each ICESat ground track profile. Then the freeboard data from profiles in each campaign period are interpolated to a $50 \times 50 \text{ km}$ grid in the Weddell Sea. The interpolation procedure is described in detail by *Zwally et al.* [1990]. For each grid cell, data are averaged within a circle with a 35 km radius. If no data are found in a circle, a radius of 100 km is used. To eliminate the effect of icebergs, freeboards greater than 1 m

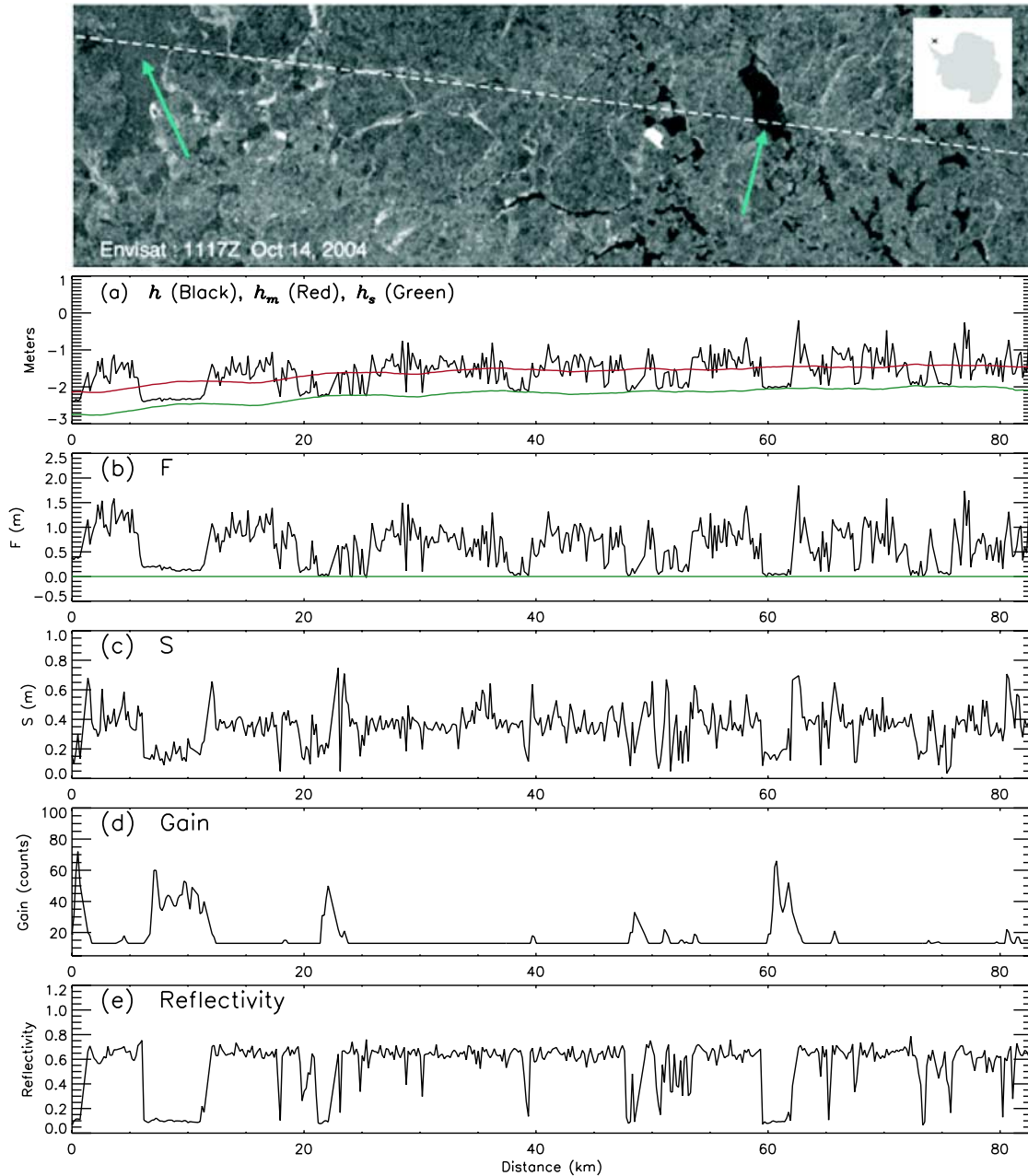


Figure 8. Near-coincident Envisat image and ICESat profile. Image is at 1117Z, 14 October 2004, and the profile is at 2302Z, 13 October 2004. ICESat ground track is shown as a dashed line. An “x” marks the approximate geographic location of the image and the ICESat profile. Flight direction is from left to right: (a) h , h_m , and h_s ; (b) freeboard; (c) pulse-broadening parameter S ; (d) detector gain; (e) reflectivity. (Envisat image: copyright ESA 2007).

are removed before gridding. The freeboards for the four periods studied are shown in Figure 9. The distributions of the freeboards show distinct differences between the May–June and October–November periods for both 2004 and 2005. In May–June, freeboards increased westward across the Weddell Sea, with larger values near the Antarctic Peninsula coast; the mean freeboard for 2004 and 2005 were 0.28 and 0.29 m. In October–November, the mean freeboard increased to 0.37 and 0.35 m for 2004 and 2005. The differences of the mean freeboards between 2004 and 2005 are 0.01 m for the May–June period and 0.02 m for the

October–November period. The spatial pattern is the same: freeboard increases westward with larger values along the Antarctic Peninsula coast. The C-shaped freeboard distribution in October–November 2004 is an expression of the large-scale sea ice circulation pattern discussed later. All freeboard histograms in Figure 9 show an asymmetrical distribution with a sharp increase in the leading edge and a slow decrease in the tail of the distribution. The mode in the histogram for the May–June periods is about 0.18 m, which is $\sim 60\%$ of the mean freeboard. In the October–November

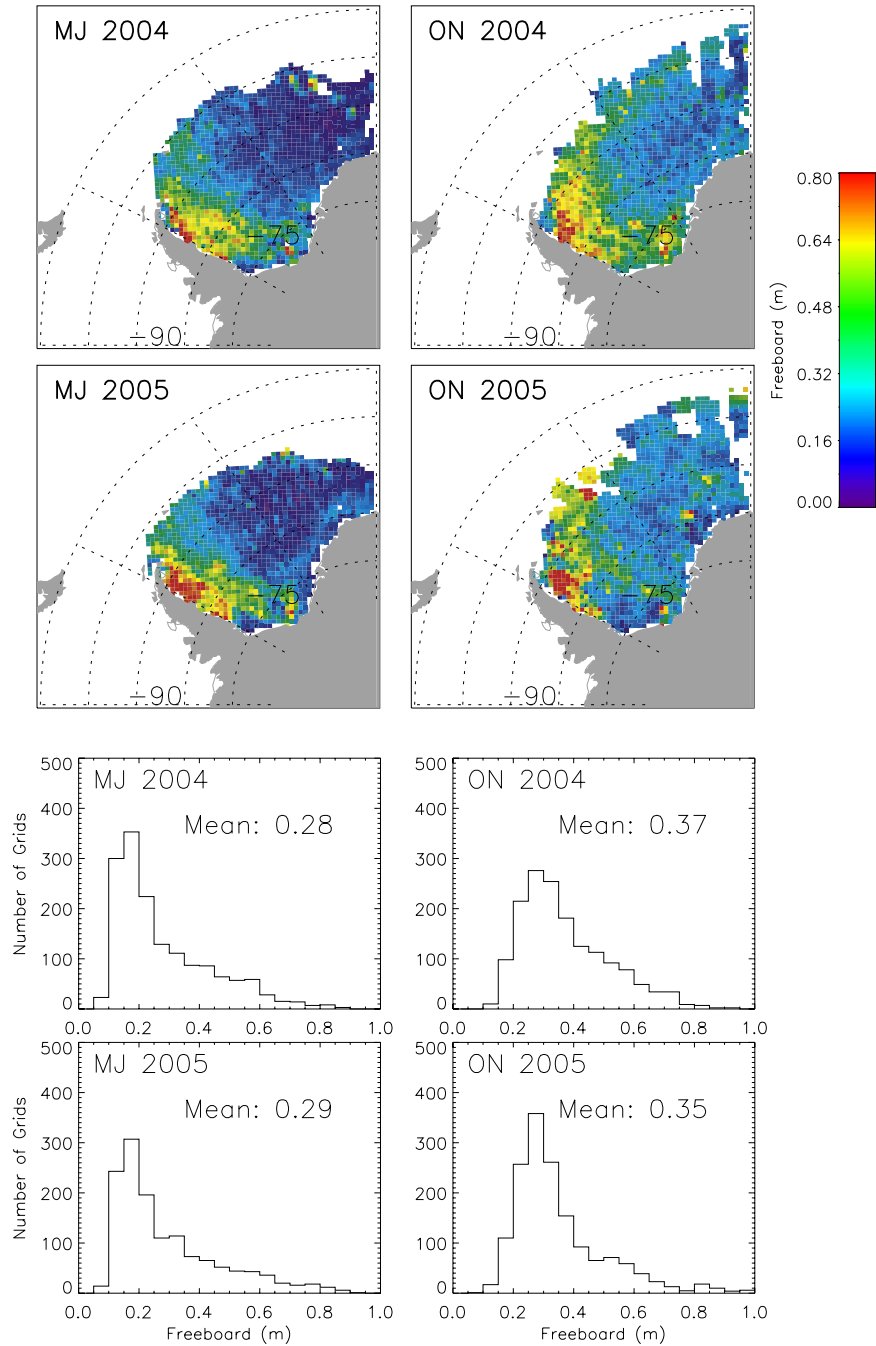


Figure 9. Freeboard maps (50×50 km grid) and histograms of the four periods. Mean freeboards for the four periods are 0.28, 0.37, 0.29, and 0.35 m. Respective modes are 0.18, 0.28, 0.18, and 0.28 m. Respective standard deviations of the means are 0.004, 0.004, 0.005, and 0.004 m.

periods the mode in the histogram is about 0.28 m, $\sim 80\%$ of the mean freeboard.

[31] Since the AMSR-E snow depth estimates are only for that portion of the cell covered by ice, but not for the whole grid; that is, it excludes open water [Markus and Cavalieri, 1998], we use the product of AMSR-E snow depth and ice concentration (mean snow depth within a grid) as our snow depth of a grid in the freeboard to thickness conversion, i.e.,

$$T_s = (\text{AMSR-E snow depth}) \times (\text{AMSR-E ice concentration}).$$

[32] Sea ice thickness is calculated from the gridded freeboard (Figure 9) and AMSR-E snow depth (Figure 3) and ice concentration (Figure 4). The sea ice thickness for the four periods is shown in Figure 10. Although modified by the snow depth distribution, the overall pattern of sea ice thickness distributions are similar to freeboard distributions, i.e. increasing westward with larger values along the Antarctic Peninsula coast and the C-shaped distribution in October–November 2004. Within the 60% ice concentration isopleth, the mode of the sea ice thickness histograms are 0.7 and 0.8 m for the May–June periods and 0.8 and 1.6 m

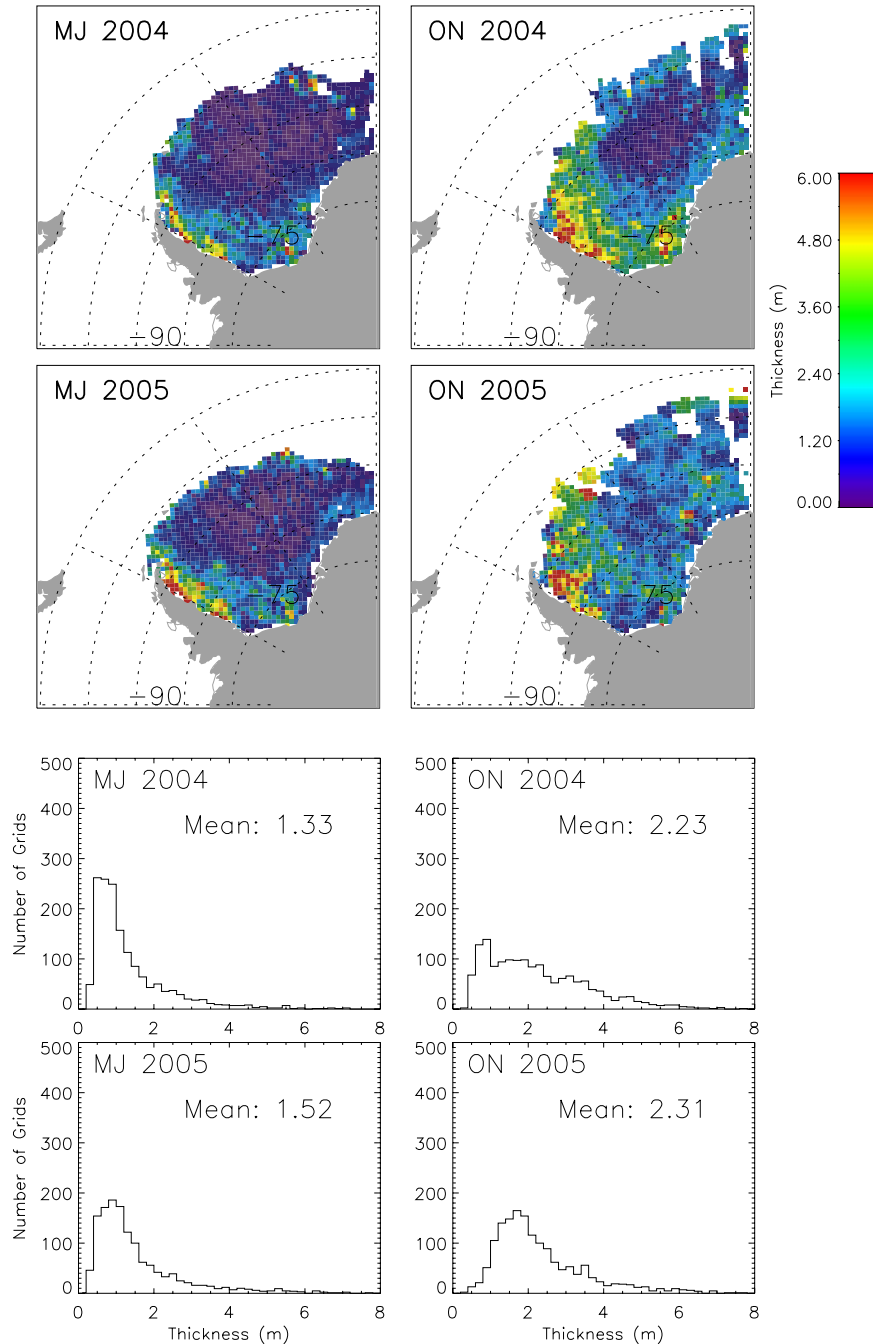


Figure 10. Thickness maps (50 × 50 km grid) and histograms of the four periods. Mean thicknesses for the four periods are 1.33, 2.23, 1.52, and 2.31 m. Respective modes are 0.7, 0.8, 0.8, and 1.6 m.

for the October–November periods. Similarly, the mean sea ice thicknesses are 1.33 and 1.52 m for the May–June periods and 2.23 and 2.31 for the October–November periods. The sea ice volumes for the two May–June periods are 5069 and 5095 km³ and, for the two October–November periods, 8574 and 8758 km³. From May–June to October–November, sea ice volume increased 70% in both years. The sea ice areas for the two May–June periods are 3.80 and 3.34 million km² and, for the two October–November periods, 3.82 and 3.78 million km².

[33] For comparison, published data on sea ice freeboard and thickness in the Weddell Sea is very limited, and there

is no data coincident with the four ICESat campaigns. Some information is provided by ship-based measurements from *Wadhams et al.* [1987] and *Lange and Eicken* [1991] in the late 1980s. For a period of 2 months between 18 July to 10 September in 1986, *Wadhams et al.* [1987] measured sea ice thickness by direct drilling and helicopter profiling using an impulse radar system in the east Weddell Sea (−5° to 8°E and 58° to 70°S). They found that the sea ice thickness ranges from a few centimeters to more than 5 m with a mode at 0.5 m, but cautioned that there were expected biases in their sampling that would underestimate the amount of thick ridges. They concluded the undeformed

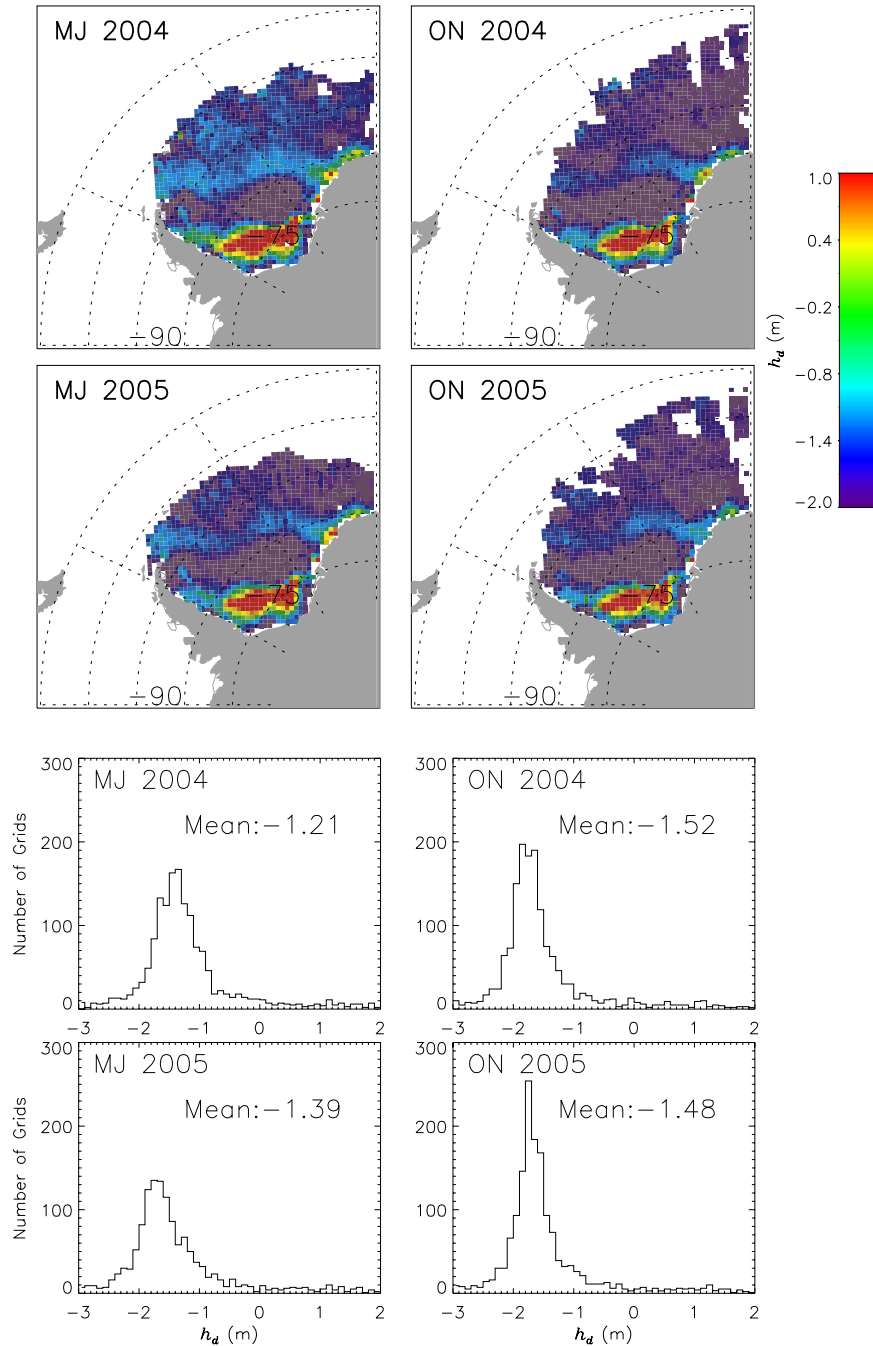


Figure 11. The h_d maps of 50×50 km grid over the four periods. Means of h_d for the four periods are -1.21 , -1.52 , -1.39 , and -1.48 m.

sea ice was concentrated in a narrow range of thickness 0.4 to 0.6 m in midwinter. These values are comparable to our results in the May–June periods; but are thinner than the October–November results, possibly because their measurement time was 1 month later than our May–June measurements and 2 months earlier than our October–November measurements. The comparison is also subject to interannual variability. *Lange and Eicken’s* [1991] sea ice thickness measurements were obtained in the northwestern Weddell Sea (-54° to -46° E and 59° to 64° S) during October to November 1989. Their overall probability density function for ice thickness reflect the complex mixture of

first-, second-, and multiyear sea ice in the northern Weddell Sea. Their sea ice thickness ranged from a few centimeters to more than 4 m with a maximum frequency at 1.3 to 1.4 m. Although there are locations with thickness less than 1 m in our October–November results in the same region, our mean thicknesses are 3.5 and 2.7 m for 2004 and 2005, more than twice their 1.3 to 1.4 m. Sampling differences, sea ice drift, measurement error, uncertainties in snow cover, and thickness changes may all contribute to these differences between satellite and field measurements.

[34] However, sampling differences are likely to be a significant factor. Characteristic features of both our free-

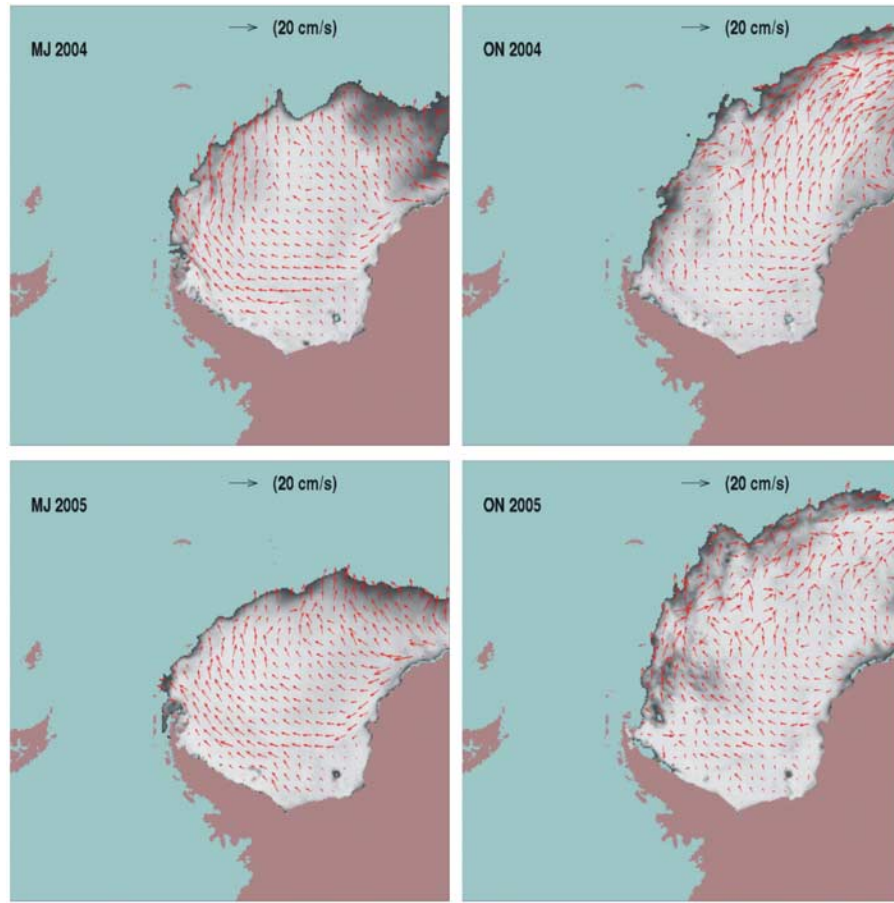


Figure 12. Mean sea ice velocity field from AMSR-E brightness temperature for the four periods. Red arrows are the direction and amplitude of the velocity. Backgrounds are ice concentration $\geq 60\%$.

board and thickness distributions (Figures 9 and 10) that may affect such comparisons are a peak at lower values than the mean and a long tail extending to 2 to 5 times the peak value. Therefore the mean value is typically greater than the most probable values, even though both values may be used to describe in some sense the average properties of the ice pack. Also, the larger values above the mean in our distributions and toward the tail are in regions of thicker ice cover that are least likely to be sampled by ship-based measurements.

5. Geoid

[35] After removing the geoid and inverted barometer effects, the elevation signal is still dominated by the unresolved geoid residuals and the dynamic surface of the ocean. Here we define the difference between ICESat measured sea level (h_s , referenced to h_m) and the EGM96 geoid (h_g) as h_d ,

$$h_d = h_m + h_s.$$

[36] In general, $h_s < 0$, so $h_d < h_m$. The h_d values for the four periods are shown in Figure 11. For all four periods, the maxima of h_d are concentrated near the Ronne Ice Shelf and the minima are just northward of the maxima. The h_d

distribution pattern is like a wave with amplitude attenuated northeastward.

[37] The spatial patterns for two different seasons and in two different years are very similar. This consistent pattern indicates that a major portion of h_d is due to time invariant factors, most likely due to uncertainties in the static geoid. The possible contributors to the time variant portion of h_d are ICESat laser pointing errors, tidal errors, and unmodeled dynamic ocean topography. The longer wavelengths of the h_d spatial features are not likely to affect the h_r calculation, since h_r is the difference between h and h_m . The average residuals between ICESat measured ocean level and the EGM96 geoid are between -1.22 and -1.53 m for the four studied periods. Further study of these residuals should improve the EGM96 geoid.

6. Ice Motion

[38] The freeboard and thickness distribution (Figures 9 and 10) in the Weddell Sea are affected by the snow depth and ice concentration. They are also affected by the ocean circulation pattern in the Weddell Sea, the Weddell Sea Gyre. The mean sea ice velocity fields derived from AMSR-E 89 GHz brightness temperature by a wavelet-transform-based sea ice tracking procedure for the four periods are shown in Figure 12. The procedure has been developed and used at the NASA/GSFC in the past several years to derive

daily Arctic sea ice motion for nonsummer seasons from satellite data, such as backscatter data from NSCAT and QuikSCAT and brightness temperature data from SSM/I and AMSR-E. The derived Arctic sea ice motion data have been shown to be in good agreements with the sea ice velocities derived from the Arctic buoy data [Liu and Cavalieri, 1998; Liu *et al.*, 1999; Zhao *et al.*, 2002, Zhao and Liu, 2007].

[39] The effect of the clockwise movement of sea ice in the Weddell Sea is most prominent in the ON 2004 period. In the southern Weddell Sea, the circulation is westward, pushing sea ice toward the Antarctic Peninsula. The freeboard is higher and the sea ice is thicker in the western Weddell Sea in all four periods studied. In the western Weddell Sea, this thicker sea ice follows the circulation northward; this is especially prominent in the two winter periods. In the northern Weddell Sea, the circulation turns eastward, indicating that the larger freeboard and thicker ice in the northern Weddell Sea are the multiyear ice from the western Weddell Sea.

7. Discussion

[40] In this section, we discuss the effect of footprint sampling, clouds, ocean swells, and snow cover on our derived freeboard values and thickness estimates. Because of ICESat's laser footprint size of 70 m and footprint spacing of 172 m, approximately 40% of the areas of open water (or thin ice) of about 70 m and larger will be measured on average. Some narrower openings may also be detected, depending on how the reflections from the mixture of open water (or thin ice) and thick ice within the footprint affect the return pulse and the Gaussian fitting. If all the points (2% over 50 km) that are used to determine the reference ocean level are open water, there is no bias in the derived freeboard. If some of the 2% points are thin ice instead of open water, there is a bias in calculated ocean level that would lead to an underestimation of the freeboard. For example, points for detected areas of 10 cm thin ice with a free board of about 1 cm could be mixed in with open water points. If all the 2% points were from 10 cm ice, the bias would therefore be about 1 cm. Therefore the bias caused by including some thin ice areas in the 2% of the points for the ocean level determination is small and is on the order of the 2 cm noise introduced by the 2 cm range precision.

[41] Clouds reduce the laser echo energy and introduce a multiple scattering delay that makes the surface appear lower. The magnitude of this delay was found to be dependant on several factors including cloud height, cloud optical depth, cloud particle size, particle shape and receiver field of view [Duda *et al.*, 2001]. ICESat measures the cloud height and cloud optical depth (when its 532 μm atmospheric channel is available), but not particle size and shape. Quantitative estimates of the cloud multiple scattering range delay is still under investigation. However, because of cloud attenuation of the laser return energy, the detector gain is strongly affected by cloud optical depth. We use an empirical gain limit to remove data affected by thick clouds. Since the transmitted pulse energy level for ON 2004, MJ 2005, and ON 2005 periods are above 35 mJ, a gain limit of 80 is used to filter out data affected by clouds. Data with gain larger than 80 counts are not used. For MJ 2004 period, the transmitted pulse energy decreased to only

6 mJ, so a gain limit of 100 counts is used; that is, data with gain higher than 100 counts are discarded.

[42] Using detector gain as a filter does not guarantee that all clouds are filtered out, especially thin clouds. Except for thin clouds, the forward scattering effect is significantly reduced. Using an even lower gain would filter out more of the data affected by clouds, but that might also filter out any low-reflectivity water and thin ice surfaces that are required to calculate mean ocean level.

[43] For the four periods MJ2004, ON2004, MJ2005, and ON2005, the numbers of points that have valid elevation measurement are 0.82, 0.68, 0.83 and 0.43 million. The number of points used in the freeboard calculation (not been filtered out by gain, reflectivity, pulse width, and elevation height limits) are 0.50, 0.50, 0.63 and 0.27 million. The percentage of points been filtered out are: 39%, 26%, 24% and 36%.

[44] Swell from the open ocean can penetrate into an ice pack in the marginal ice zone. Carsey *et al.* [1989] observed penetration distances between 5 and 150 km in the Arctic. In the Weddell Sea, ICESat data show that the penetration distance can reach up to 200 km. This phenomenon in the marginal ice zone will contaminate laser altimeter data for freeboard estimation. For this study, we choose to use data with ice concentration higher than 60% to limit the impact of ocean swell. AMSR-E ice concentration data are used to filter out low ice concentration data. Further investigation is needed to filter out ocean swell and not limit the freeboard estimation to areas with ice concentration higher than 60%.

[45] Snow accumulation on sea ice can cause flooding in the Weddell Sea. Snow ice forms from the refreezing of slush at the snow-ice interface. In some of the grid cells, AMSR-E snow depth is larger than the freeboard estimated from ICESat profiles. This may be due to measurement error or slow penetration of brine into the snow layer or both. Since the freeboard defined in this study is the height between the air-snow surface (not the snow-ice surface) and the reference ocean level, the mean freeboard is always positive. In our calculation, if snow depth is larger than freeboard, it is set equal to the freeboard. For the four periods, the percentages of area where snow depth is larger than freeboard are 26%, 13%, 13%, and <1%. The large percentage for May–June 2004 reflects a large mean snow depth (0.02 m thicker than May–June 2005), and the small percentage for October–November 2005 reflects a small mean snow depth (0.04 m thinner than October–November 2004).

[46] Snow wetness affects the dielectric properties of snow and biases snow depth from passive microwave sensors to smaller values [Markus and Cavalieri, 1998]. It is possible that the apparently thinner snow cover in the October–November 2005 period (see Figure 3) is due to melting, since this period is more than two weeks later in the year than the October–November 2004 period. If this were so, it would explain the thicker sea ice derived from ICESat for the same period (see Figure 10).

[47] The techniques used here require further development and analysis. A future cloud-detecting method based on the ICESat 1064 μm atmospheric channel data will improve cloud detection for all campaign periods, so clouds can be filtered out without using the detector gain limit. This should reduce the chance of open water and thin ice data being removed and improve the reference ocean level

calculation. Future laboratory tests leading to better saturation corrections should improve the elevation precision for saturated waveforms; it may also improve the saturation correction for heavily saturated waveform and make elevations associated with those waveforms useful, hence improving the derived freeboard.

8. Conclusions

[48] This is a first examination of using ICESat elevation profiles to derive sea ice freeboards in the Weddell Sea. Estimates of snow depth on the sea ice from AMSR-E passive microwave data, along with nominal densities of snow, water, and sea ice, are used to estimate sea ice thickness. This study demonstrates that ICESat provides a unique capability for measuring sea ice freeboards with complete basin-scale coverage on approximately monthly timescales. For sea ice thickness it is a first assessment of thickness obtained from the derive freeboards using nominal densities and satellite snow cover estimates.

[49] AMSR-E snow depth estimates over the southern ocean are the only basin-scale snow depth data available. Uncertainties in snow depth and density introduce uncertainties in sea ice thickness estimates. Better snow depth and snow density data are needed to improve sea ice thickness calculated from ICESat sea ice freeboard. Additional in situ measurements such as sea ice freeboard, thickness, snow depth, and snow density coincident with ICESat and AMSR-E measurements are necessary to further calibrate/validate the snow depth, freeboard, and thickness results. Validation is difficult with pointwise measurements in the presence of ice drift, but we should be able to do better with coordinated field experiments with both airborne and ground-based observations.

[50] In each of its 33-d operating periods, ICESat covers the entire Southern Ocean with 500 ground tracks. Clearly, this coverage offers great promise for monitoring sea ice in the entire Southern Ocean. These observations from satellites will be made more credible as they can be more thoroughly compared with new in situ observations, such as those made by ships [Ackley, 1979; Wadhams et al., 1987].

[51] The ocean levels derived from ICESat elevation profiles over sea ice quantify the large errors in current geoid model on average. Their temporal variations may be due to errors in the tide model and temporal variations in the dynamic topography.

[52] The seasonal changes and the interannual values and distributions of the ICESat derived freeboards show a year-to-year consistency, spatial distributions that appear realistic, and a realistic seasonal growth during the winter months. For example, the spatial distribution shows the characteristic thick ice near the Antarctic Peninsula, with thicker ice toward the north and extending to the East in a pattern that is consistent with the drift and growth of thicker ice in the Weddell gyre. Thinner ice is located in the region of new ice formation in front of the Filchner and Ronne Ice Shelves, and in the inner part of the gyre. The growth of the mean freeboard of about 6 to 9 cm from May–June to October–November appears realistic and corresponding estimated growth in mean thickness of 80 to 90 cm is also realistic. Continued measurements by satellite laser altim-

eters will reveal seasonal and annual variations of sea ice thickness and volume, which are critical indicators of climate change.

[53] **Acknowledgments.** We thank Alvaro Ivanoff, Donald J. Cavalieri, and Steve Fiegles for their assistance with the AMSR-E data. We thank Brian Beckley for his assistance with inverse barometer correction calculation. We also thank Thorsten Markus and Joey Comiso for their help on the understanding of AMSR-E snow depth and ice concentration data. This work is supported by NASA's funding of the ICESat Project Science and the ICESat Science Team.

References

- Abshire, J. B., X. Sun, H. Riris, J. M. Sirota, J. F. McGarry, S. Palm, D. Yi, and P. Liiva (2005), Geoscience Laser Altimeter System (GLAS) on the ICESat mission: On-orbit measurement performance, *Geophys. Res. Lett.*, **32**, L21S02, doi:10.1029/2005GL024028.
- Ackley, S. F. (1979), Mass-balance aspects of Weddell Sea pack ice, *J. Glaciol.*, **24**(90), 391–405.
- Bamber, J. L., and R. Kwok (2004), Remote-sensing techniques, in *Mass Balance of the Cryosphere: Observations and Modeling of Contemporary and Future Changes*, edited by J. L. Bamber and A. J. Payne, pp. 59–113, Cambridge Univ. Press, New York.
- Carsey, F. D., S. A. D. Argus, M. J. Collins, B. Holt, C. E. Livingstone, and C. L. Tang (1989), Overview of LIMEX'87 ice observations, *IEEE Trans. Geosci. Remote Sens.*, **27**(5), 468–482.
- Comiso, J. C., D. J. Cavalieri, and T. Markus (2003), Sea-ice concentration, ice temperature, and snow depth using AMSR-E data, *IEEE Trans. Geosci. Remote Sens.*, **41**(2), 243–252.
- Dorandeu, J., and P. Y. Le Traon (1999), Effects of global mean atmospheric pressure variations on mean sea level changes from TOPEX/POSEIDON, *J. Atmos. Oceanic Tech.*, **16**(9), 1279–1283.
- Drinkwater, M. R., and V. I. Lytle (1997), ERS 1 radar and field-observed characteristics of autumn freeze-up in the Weddell Sea, *J. Geophys. Res.*, **102**(C6), 12,593–12,608.
- Drinkwater, M. R., X. Liu, and S. Harms (2001), Combined satellite and ULS-derived sea-ice flux in the Weddell Sea, Antarctica, *Ann. Glaciol.*, **33**, 125–132.
- Duda, D. P., J. D. Spinhrne, and E. W. Eloranta (2001), Atmospheric multiple scattering effects on GLAS altimetry. part I: Calculations of single pulse bias, *IEEE Trans. Geosci. Remote Sens.*, **39**(1), 92–101.
- Geiger, C. A., and M. R. Drinkwater (2005), Coincident buoy- and SAR-derived surface fluxes in the western Weddell Sea during Ice Station Weddell 1992, *J. Geophys. Res.*, **110**, C04002, doi:10.1029/2003JC002112.
- Gloersen, P., W. J. Campbell, D. J. Cavalieri, J. C. Comiso, C. L. Parkinson, and H. J. Zwally (1992), *Arctic and Antarctic Sea Ice, 1978–1987: Satellite Passive-Microwave Observations and Analysis*, NASA SP-511, 290 pp.
- Hartmann, J., C. Kottmeier, C. Wamser, and E. Augstein (1994), Aircraft measured atmospheric momentum, heat and radiation fluxes over Arctic sea ice, in *The Polar Oceans and Their Role in Shaping the Global Environment: The Nansen Centennial Volume*, *Geophys. Monogr. Ser.*, vol. 85, edited by O. M. Johannessen, R. D. Meunch, and J. E. Overland, pp. 443–454, AGU, Washington, D. C.
- Kwok, R. (2005), Ross Sea ice motion, flux, and deformation, *J. Clim.*, **18**(18), 3759–3776.
- Kwok, R., and J. C. Comiso (2002), Southern ocean climate and sea ice anomalies associated with the Southern Oscillation, *J. Clim.*, **15**(5), 487–501.
- Kwok, R., H. J. Zwally, and D. Yi (2004), ICESat observations of Arctic sea ice: A first look, *Geophys. Res. Lett.*, **31**, L16401, doi:10.1029/2004GL020309.
- Kwok, R., G. F. Cunningham, H. J. Zwally, and D. Yi (2006), ICESat over Arctic sea ice: Interpretation of altimetric and reflectivity profiles, *J. Geophys. Res.*, **111**, C06006, doi:10.1029/2005JC003175.
- Lange, M. A., and H. Eicken (1991), The sea ice thickness distribution in the northwestern Weddell Sea, *J. Geophys. Res.*, **96**(C3), 4821–4837.
- Laxon, S., N. Peacock, and D. Smith (2003), High interannual variability of sea ice thickness in the Arctic region, *Nature*, **425**, 947–950.
- Lindsay, R. W., and D. A. Rothrock (1995), Arctic sea ice leads from advanced very high resolution radiometer images, *J. Geophys. Res.*, **100**(C3), 4533–4544.
- Liu, A. K., and D. J. Cavalieri (1998), Sea-ice drift from wavelet analysis of DMSP SSM/I data, *Int. J. Remote Sens.*, **19**, 1415–1423.
- Liu, A. K., Y. Zhao, and S. Y. Wu (1999), Arctic sea ice drift from wavelet analysis of NSCAT and SSM/I data, *J. Geophys. Res.*, **104**(C5), 11,529–11,538.

- Mahesh, A., J. D. Spinhirne, D. P. Duda, and E. W. Eloranta (2002), Atmospheric multiple scattering effects on GLAS altimetry. part II: Analysis of expected errors in Antarctic altitude measurements, *IEEE Geosci. Remote Sens.*, 40(11), 2353–2362.
- Markus, T., and D. J. Cavalieri (1998), Snow depth distribution over sea ice in the Southern Ocean from satellite passive microwave data, in *Antarctic Sea Ice: Physical Process, Interactions and Variability*, *Antarct. Res. Ser.*, vol. 74, pp. 19–39, AGU, Washington, D. C.
- Minson, D. G. (1990), Evolution of the Southern Ocean winter mixed layer and sea ice: Open ocean deepwater formation and ventilation, *J. Geophys. Res.*, 95(C7), 11,641–11,654.
- Massom, R. A., M. R. Drinkwater, and C. Haas (1997), Winter snow cover on sea ice in the Weddell Sea, *J. Geophys. Res.*, 102(C1), 1101–1118.
- Picot, N., K. Case, S. Desai, and P. Vincent (2003), *AVISO and PODAAC User Handbook, IGDR and GDR Jason Products, SMM-MU-M5-OP-13184-CN(AVISO), JPL D-21352 (PODAAC)*, Jet Propul. Lab., Calif. Inst. of Technol., Pasadena, Calif. (Available at http://podaac.jpl.nasa.gov/jason/documents/Handbook_Jason.pdf)
- Ray, R. D. (1999), A global ocean tide model from TOPEX/Poseidon altimetry: GOT99.2, *NASA Tech. Memo.*, 209478, 58 pp.
- Rothrock, D. A., Y. Yu, and G. A. Maykut (1999), Thinning of the Arctic sea-ice cover, *Geophys. Res. Lett.*, 26(23), 3469–3472.
- Schutz, B. E., H. J. Zwally, C. A. Shuman, D. Hancock, and J. P. DiMarzio (2005), Overview of the ICESat Mission, *Geophys. Res. Lett.*, 32, L21S01, doi:10.1029/2005GL024009.
- Shuman, C. A., H. J. Zwally, B. E. Schutz, A. C. Brenner, J. P. DiMarzio, V. P. Suchdeo, and H. A. Fricker (2006), ICESat Antarctic elevation data: Preliminary precision and accuracy assessment, *Geophys. Res. Lett.*, 33, L07501, doi:10.1029/2005GL025227.
- Stackpole, J. D. (1993), The WMO format for the storage of weather product information and the exchange of weather product messages in gridded binary form, *NOAA Office Note 388*, 79 pp., Natl. Oceanic and Atmos. Admin., Washington, D. C.
- Strass, V. H., and E. Fahrbach (1998), Temporal and regional variation of sea ice draft and coverage in the Weddell Sea obtained from upward looking sonars, in *Antarctic Sea Ice: Physical Process, Interactions and Variability*, *Antarct. Res. Ser.*, vol. 74, edited by M. O. Jeffries, pp. 123–139, AGU, Washington, D. C.
- Sturm, M., K. Morris, and R. Massom (1998), The water snow cover of the west Antarctic pack ice: Its spatial and temporal variability, *Antarct. Res. Ser.*, vol. 74, edited by M. O. Jeffries, pp. 1–18, AGU, Washington, D. C.
- Sun, X., J. B. Abshire, and D. Yi (2003), Geoscience Laser Altimeter System (GLAS): Characteristics and performance of the altimeter receiver, *EOS Trans. AGU*, 84(46), Fall Meeting Suppl., Abstract C32A-0432.
- Tin, T., and M. O. Jeffries (2001), Sea-ice thickness and roughness in the Ross Sea, Antarctica, *Ann. Glaciol.*, 33, 187–193.
- Wadhams, P., M. A. Lange, and S. F. Ackley (1987), The ice thickness distribution across the Atlantic sector of the Antarctic Ocean in midwinter, *J. Geophys. Res.*, 92(C13), 14,535–14,552.
- Worby, A. P., G. M. Bush, and I. Allison (2001), Seasonal development of the sea-ice thickness distribution in East Antarctica: Measurements from upward-looking sonar, *Ann. Glaciol.*, 33, 177–180.
- Yi, D., X. Sun, and H. J. Zwally (2003), A study of the GLAS echo waveform using ground test data, *Geophys. Res. Abstr.*, 5, 13690.
- Yi, D., H. J. Zwally, and X. Sun (2005), ICESat measurement of Greenland Ice Sheet surface slope and roughness, *Ann. Glaciol.*, 42, 83–89.
- Zhao, Y., and A. K. Liu (2007), Arctic sea-ice motion and its relation to pressure field, *J. Oceanogr.*, 63, 505–515.
- Zhao, Y., A. K. Liu, and D. G. Long (2002), Validation of sea ice motion from QuikSCAT with those from SSM/I and buoy, *IEEE Trans. Geosci. Remote Sens.*, 40, 1241–1246.
- Zwally, H. J., A. C. Brenner, J. A. Major, and R. A. Bindshadler (1990), Satellite radar altimetry over ice, *NASA Ref. Pub.*, 1233, vol. 1, section 5.0, 47–54.
- Zwally, H. J., et al. (2002a), ICESat's laser measurements of polar ice, atmosphere, ocean, and land, *J. Geodyn.*, 24, 405–445.
- Zwally, H. J., J. C. Comiso, C. L. Parkinson, D. J. Cavalieri, and P. Gloersen (2002b), Variability of Antarctic sea ice 1979–1998, *J. Geophys. Res.*, 107(C5), 3041, doi:10.1029/2000JC000733.

R. Kwok, Jet Propulsion Laboratory, California Institute of Technology, 4800 Oak Grove Drive, Pasadena, CA 91109, USA.

D. Yi, SGT, Incorporated, Cryospheric Sciences Branch, Code 614.1, Goddard Space Flight Center, Greenbelt, MD 20771, USA. (donghui.yi@nasa.gov)

Y. Zhao, Caelum Research Corporation, Oceans Sciences Branch, Code 614.2, Goddard Space Flight Center, Greenbelt, MD 20771, USA.

H. J. Zwally, Cryospheric Sciences Branch, Code 614.1, Goddard Space Flight Center, Greenbelt, MD 20771, USA.